BIOCHEMISTRY
including biophysical chemistry & molecular biology

ARTICLE

pubs.acs.org/biochemistry

Quantitative Measurement of Ca^{2+}-Dependent Calmodulin−Target Binding by Fura-2 and CFP and YFP FRET Imaging in Living Cells

Masayuki X. Mori,*[,†] Yuko Imai,[†,‡] Kyohei Itsuki,[†,‡] and Ryuji Inoue[†]

[†]Department of Physiology, School of Medicine, Fukuoka University, Fukuoka, Japan

[‡]Faculty of Dental Science, Kyushu University, Fukuoka, Japan

Supporting Information

ABSTRACT: Calcium dynamics and its linked molecular interactions cause a variety of biological responses; thus, exploiting techniques for detecting both concurrently is essential. Here we describe a method for measuring the cytosolic Ca^{2+} concentration ($[Ca^{2+}]_i$) and protein−protein interactions within the same cell, using Fura-2 and superenhanced cyan and yellow fluorescence protein (seCFP and seYFP, respectively) FRET imaging techniques. Concentration-independent corrections for bleed-through of Fura-2 into FRET cubes across different time points and $[Ca^{2+}]_i$ values allowed for an effective separation of Fura-2 cross-talk signals and seCFP and seYFP cross-talk signals, permitting calculation of $[Ca^{2+}]_i$ and FRET with high fidelity. This correction approach was particularly effective at lower $[Ca^{2+}]_i$ levels, eliminating bleed-through signals that resulted in an artificial enhancement of FRET. By adopting this correction approach combined with stepwise $[Ca^{2+}]_i$ increases produced in living cells, we successfully elucidated steady-state relationships between $[Ca^{2+}]_i$ and FRET derived from the interaction of seCFP-tagged calmodulin (CaM) and the seYFP-fused CaM binding domain of myosin light chain kinase. The $[Ca^{2+}]_i$ versus FRET relationship for voltage-gated sodium, calcium, and TRPC6 channel CaM binding domains (IQ domain or CBD) revealed distinct sensitivities for $[Ca^{2+}]_i$. Moreover, the CaM binding strength at basal or subbasal $[Ca^{2+}]_i$ levels provided evidence of CaM tethering or apoCaM binding in living cells. Of the ion channel studies, apoCaM binding was weakest for the TRPC6 channel, suggesting that more global Ca^{2+} and CaM changes rather than the local CaM−channel interface domain may be involved in Ca^{2+}CaM-mediated regulation of this channel. This simultaneous Fura-2 and CFP- and YFP-based FRET imaging system will thus serve as a simple but powerful means of quantitatively elucidating cellular events associated with Ca^{2+}-dependent functions.

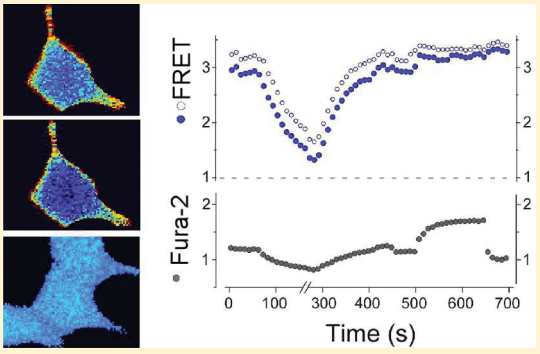

Numerous ion channels are known to be modulated by calmodulin (CaM),[1] which mediates cytosolic Ca^{2+} signals to control channel activity in diverse physiological contexts. CaM, a small ubiquitous protein, contains four EF-hand Ca^{2+} binding sites and activates a wide variety of cellular functions through its direct interaction with enzymes, cytoskeletal proteins, and ion channels.[2] It is relatively well-known from steady-state Ca^{2+}-dependent CaM−target binding experiments that CaM specifically binds distinct enzymes at different Ca^{2+} concentrations.[3] This variability in the Ca^{2+} dependence of formation of the CaM complex with enzymes likely contributes significantly to the diversity and versatility of Ca^{2+} signaling. However, such information is still scanty for ion channels, where tethering of Ca^{2+} free apoCaM is thought to play a role equally critical to that of Ca^{2+}-dependent CaM binding, because the latter process may be too slow to account for ion channel processes with fast kinetics such as single-channel events. For example, tethering of CaM (presumably apoCaM binding) to the IQ domain of L-type Ca channels is shown to be requisite for its inactivation at both macroscopic and single-channel current levels.[4,5]

Recent studies have pointed out that dysfunctional or chronic elevation of the basal cytosolic Ca^{2+} concentration ($[Ca^{2+}]_i$) may lead to pathological cellular states manifested as cardiac hypertrophy,[6] Alzheimer's disease,[7] and inflammatory bowel disease.[8] Therein, CaM may be inappropriately bound to ion channels because of pathologically elevated $[Ca^{2+}]_i$ levels, thereby producing excessive or abnormal cellular responses. Thus, it is of great significance to exploit a quantitative method for visualizing Ca^{2+} dynamics and concomitant ion channel−CaM interactions in the same living cells.

FRET measurements with green fluorescent protein (GFP) derivatives, between CFP [or Cerulean, CPet, or seCFP (donor)] and YFP [or Venus, Citrine, YPet, or seYFP (acceptor)], have been widely used to detect protein−protein interactions, where in most cases, both flurophores are coexpressed in the same cell as fusion proteins to molecules of interest.[9] This technique, when combined

Received: February 24, 2011
Revised: April 21, 2011
Published: April 25, 2011

with appropriate corrections for cross-talk among fluorescence spectra, ensures the quantitative evaluation of intermolecular interactions, as exemplified by three-cube FRET methods.[9−11] For cytosolic Ca^{2+} imaging, Fura-2 has fewer overlaps in both excitation and emission spectra with CFP and YFP FRET (C/Y FRET), as compared with other Ca^{2+} fluorescent dyes. This Ca^{2+} indicator is even better for minimizing contamination of autofluorescence from the cells compared with Indo-1, another suitable Ca^{2+} dye for C/Y FRET.[12] Wier et al.[13] and Harbeck et al.[14] have closely examined cross-talk between the excitation spectra of the C/Y FRET pair and Fura-2 and concluded that it was practically negligible. However, the degree of cross-talk varies depending on specific conditions, including filter sets, the loading concentration of Fura-2, the expression level of FRET constructs, and $[Ca^{2+}]_i$.[15] Thus, even a small degree of cross-talk could possibly obfuscate the true Fura-2 or FRET ratio, especially when the change is subtle.

To solve this "cross-talk" problem that is detected as bleed-through, we have developed a quantitative simultaneous imaging method for Fura-2 and C/Y FRET in single living cells by sequential capturing of each signal. To facilitate this, we have used two major technical devices. (1) We used the F_{340}/F_{360} ratio. Despite a broader dynamic range for F_{340}/F_{380} than for F_{340}/F_{360}, the former is prone to the contamination of seCFP fluorescence directly excited at 380 nm. To reduce the level of this contamination, the F_{340}/F_{360} ratio was used as an indicator of $[Ca^{2+}]_i$. (2) We used correction of Ca^{2+}-dependent Fura-2 fluorescence bleed-through on FRET images. Dynamic changes in $[Ca^{2+}]_i$ shift the excitation spectra of Fura-2 toward or away from those of seCFP and seYFP, causing different degrees of spectral overlap (Figure 1A). This in turn introduces variable degrees of errors in the calculation of the FRET efficiency at each time point. To minimize this type of error, we subtracted Fura-2 bleed-through signals from the corresponding seCFP, seYFP, and FRET signals, using their calibration curves that were preconstructed with respect to various F_{340}/F_{360} ($[Ca^{2+}]_i$) values (Figure 1C).

After constructing the calibration curves, we applied them to evaluate steady-state relationships between $[Ca^{2+}]_i$ and the interaction of CaM with smooth muscle myosin light chain kinase peptide (smMLCKp) in living cells. Moreover, we confirmed the validity of evaluating the macroscopic Ca^{2+} sensitivity of CaM by this method, using various CaM mutants known to form distinct Ca^{2+}-dependent complexes.

We finally attempted to account for the target-specific Ca^{2+}-dependent interactions of CaM with various types of ion channels. Ion channels have been intensively investigated for their CaM-mediated regulation in gating and membrane trafficking over the past decade,[1] but their precise Ca^{2+} dependence, apoCaM binding, and resultant functional modification still remain largely unclear.

EXPERIMENTAL PROCEDURES

Molecular Engineering. Enhanced CFP and YFP variants superenhanced CFP (seCFP) and superenhanced YFP (seYFP) were isolated from the Rho GTPase activity biosensor "Raichu" (provided by M. Nakaya, Kyushu University) and then mutated to generate monomeric fluorescence proteins (A206K) with polymerase chain reaction-mediated overlap extension using mutagenic primers.[16] Thus, seYFP and seCFP contain F64L, M153T, V163A, S175G, and A206K mutations and F64L, M153T, V163A, S175G, and A206K mutations, respectively. Both seCFP and seYFP display fluorescence spectra identical to those of eCFP and eYFP, respectively.[17,18] For the construction of fluorophore-tagged molecules, seCFP was fused to the N-terminus of rat wild-type CaM (CaM_{wt}, NP_059022) or mutants of

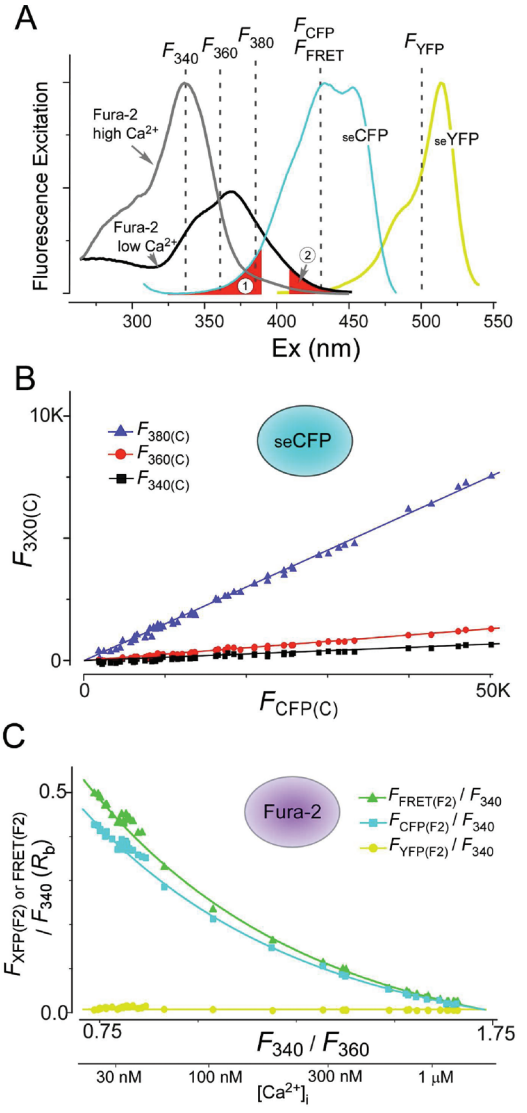

Figure 1. Cross-talk between Fura-2 and CFP and YFP molecules. (A) Excitation spectra for Fura-2 at high and low Ca^{2+} concentrations (black and gray lines, respectively), seCFP (cyan), and seYFP (yellow). Overlapping and problematic areas are colored red (regions 1 and 2). The dashed lines labeled F_X (X = 340, 360, 380, CFP, YFP, or FRET) denote the respective excitation wavelengths. (B) Intensity of seCFP fluorescence induced by Fura-2 excitation wavelengths [$F_{340(C)}$, $F_{360(C)}$, and $F_{380(C)}$] plotted vs that induced by the seCFP excitation wavelength [$F_{CFP(C)}$] obtained from the same cell. No significant emission was detected from seYFP-expressing cells with Fura-2 excitation (data not shown). (C) Appearance of Ca^{2+}-dependent Fura-2 bleed-through onto FRET images. Fura-2-loaded cells (without XFP) were illuminated with three FRET cubes [$F_{CFP(F2)}$, $F_{YFP(F2)}$, and $F_{FRET(F2)}$] at various $[Ca^{2+}]_i$ levels (F_{340}/F_{360}, x-axis). Ca^{2+}-dependent bleed-through ratios (R_b, y-axis) of FRET images to F_{340} values, which were approximated by single-exponential fitting [data for $F_{CFP(F2)}$, $F_{YFP(F2)}$, and $F_{FRET(F2)}$ are colored green, cyan, and yellow, respectively]. The values of the estimated free Ca^{2+} concentration ($[Ca^{2+}]_i$) are displayed along with the Fura-2 ratio.

CaM, such as CaM_{m1234} (four point mutations in four EF-hands, provided by D. T. Yue, Johns Hopkins University, Baltimore, MD). seYFP was also fused to the N-terminus of the CaM target region from human smooth muscle myosin light chain kinase (smMLCK, provided by S. Shimizu, Showa University, Tokyo, Japan), rat voltage-gated Na channel $Na_V1.2$ (NP_036779.1, provided by M. Noda, National Institute for Basic Biology, Okazaki, Japan), voltage-gated Ca channel $Ca_V2.1$ (NP_000059.3) and $Ca_V1.2$ (1512308A) (provided by D. T. Yue), or transient receptor potential (TRP) channel TRPC6 (CAA06943.1, provided by T. Hoftmann, Philipps-Universität Marburg, Marburg, Germany) by polymerase chain reaction amplification. The amino acid sequences of CaM target regions are summarized in the Supporting Information. The resulting linker separating a fluorescence protein and CaM or its targets was an alanine triplet (AAA). A seCFP−seYFP dimeric molecule was constructed from seCFP and seYFP molecules linked with a tetraglycine linker (GGGG). Fluorophore-tagged CaM, CaM target segments, and the seCFP−seYFP dimer were subcloned into expression vector pIRES2n that was modified from vector pIRES2 (Invitrogen) via deletion of the IRES to eGFP coding region.

Cell Culture and Transfection. Human embryonic kidney 293 (HEK293) cells (purchased from American Type Culture Collection, Manassas, VA) were maintained in Dulbecco's modified Eagle's medium (DMEM) supplemented with 10% fetal bovine serum with antibiotics (Penn/Strep, Gibco). For transfection, the cells were reseeded onto poly-L-lysin-coated coverslips (thickness of 0.06−0.08 mm, Matsunami) placed in a 24-well culture plate and then transfected with a mixture of 1 μg of plasmid vector incorporating DNAs, with the aid of Fugene 6 reagent (Roche). Imaging was performed within 24−36 h of transfection to avoid enhancement of autofluorescence and extraordinarily strong overexpression.

Fura-2 and C/Y FRET Measurements. A glass coverslip with transfected HEK cells was incubated for 30 min at 37 °C with 5 μM Fura-2/AM (Molecular Probes, Eugene, OR) and 0.1% pluronic acid F-127 (Sigma) in a HEPES-buffered solution composed of 140 mM NaCl, 5 mM KCl, 1.2 mM $MgCl_2$, 1 mM $CaCl_2$, 10 mM HEPES, and 10 mM glucose (pH 7.4, adjusted with Tris base). The coverslip was then washed with HEPES-buffered solution and placed in a glass dish chamber on an inverted microscope (DMI 6000 B, Leica Inc., Herbrug, Switzerland) equipped with a 40× oil immersion objective lens (Leica, PL Fluotar, NA 1.00). Two Fura-2 images were obtained by alternate illumination of a 175 W xenon arc lamp at 340 nm (D340/20, Chroma, Rockingham, VT) and 360 nm (D360/10, XB60 360BP10, Omega Optical, Brattleboro, VT) excitation wavelengths, by means of a computer-controlled high-speed wavelength-switching light source (Lambda DG-4, Sutter Instrument Co., Novato, CA). For comparison, a 380 nm excitation filter (D380/20, Chroma) was also tested (utilized only for Figure 1B). Emitted fluorescence was reflected through a Fura-2 cube (410DCLP, D510/80M, Chroma). Three FRET images (cube settings for CFP, YFP, and FRET) were obtained from a direct light passing window of the wheel DG-4 to three FRET cubes (excitation, dichroic, and emission): CFP (D435/20M, 455DCLP, D480/30M, Leica), YFP (D500/25, 515DCLP, D535/30M, Leica), and FRET (D435/20M, 455DCLP, D535/30M, Leica). Fura-2 and FRET cubes were sequentially rotated with a motorized instrument (rotation period for each of the filter cubes was ~0.8 s), and all images (two and three for Fura-2 and C/Y FRET, respectively) were obtained within 3.5 s every 10 s. Each of the images was captured on a cooled 16-bit CCD camera (QuantEM512, Roper Scientific, Trenton, NJ) with an exposure time of 100 ms with 1 × 1 binning (total of 512 × 512 pixels) under the control of Slidebook version 4.2 (Intelligent Imaging Innovations, Denver, CO). To obtain the averaged intensity of a cytosolic sample, 10 × 10 pixels were selected within a cell (which is roughly 10−50% of the total cell area) using custom software written in MATLAB (MathWorks, Natick, MA). We confirmed that a pixel shift problem during image capturing is almost negligible by our averaging calculation approach. Further data processing and curve fitting were performed with Excel (Microsoft, Bellevue, WA).

Nomenclature for Various Fluorescence Measurements. The actual fluorescence signal output obtained from a given sample with a certain optical filter setting or cube is denoted by the descriptor F_X(fluorophore), where X is the name of the filter setting or the cube (340, 360, CFP, YFP, or FRET) and the fluorophore is either Fura-2 (F2) seCFP(C), or seYFP(Y). For example, the signal output obtained from Fura-2, seCFP, and seYFP with the CFP cube is expressed as $F_{CFP(F2,C,Y)}$. However, there is virtually no seCFP or seYFP bleed-through from the Fura-2 filter settings (shown in Figure 1B); we do define only a particular fluorophore for F_{340} and F_{360} in Figure 1B. Averaged background signals calculated from a couple of non-C/Y-transfected and -Fura-2/AM-loaded cells for each image (i.e., F_{340}, F_{360}, F_{CFP}, F_{YFP}, and F_{FRET}) were presubtracted from each actual image before the Fura-2 and FRET measurements, as described below.

Calculation Procedures Used for Corrected FR. To calculate Ca^{2+}-dependent Fura-2 bleed-through in the three FRET images (F_{CFP}, F_{YFP}, and F_{FRET}), the three corresponding calibration curves were preconstructed by the measurements from Fura-2-loaded cells without seCFP and seYFP expression. The flowing bath solution of Fura-2-loaded cells was sequentially exchanged for solutions with various Ca^{2+} concentrations with or without ionomycin to confer the calibration data points. For this purpose, cells were continuously perfused with the solutions by gravity at a flow rate of 0.5 mL/min. The "on" and "off" periods of perfusion were controlled by electromagnetic solenoid microvalves (The Lee Co., Essex, CT). We therefore were able to renew the calibration data for every new experiment or every dish from non-seCFP- or non-seYFP-transfected cells. The data obtained for Fura-2 bleed-through on FRET cubes [$F_{CFP(F2)}$, $F_{YFP(F2)}$, and $F_{FRET(F2)}$] were then normalized to that of F_{340} and plotted versus the Fura-2 ratio (F_{340}/F_{360}) (Figure 1C). To obtain the calibration curves, we then fitted these relationships with an exponential decay function by empirical least-squares fitting:

$$R_b = F_{CFP(F2)} \text{ or } F_{YFP(F2)} \text{ or } F_{FRET(F2)}/F_{340} \equiv R_o + R_{max} \times \exp[-(F_{340}/F_{360} - R_c)/R_t] \quad (1)$$

where R_o, R_{max}, R_c, and R_t denote the constants for the offset, maximum amplitude, center, and decay constants, respectively. R_b thus indicates an estimated bleed-through ratio at a particular Fura-2 ratio. Typical constants resulting from these fits are given in the Supporting Information. We then calculated Ca^2-dependent Fura-2 bleed-through [$F_{XFP(F2)calc}$] using the estimated bleed-through ratio (R_b, eq 1) at each observed F_{340}/F_{360} ratio, as follows:

$$F_{CFP(F2)calc} \text{ or } F_{YFP(F2)calc} \text{ or } F_{FRET(F2)calc} = F_{340}R_b \quad (2)$$

where F_{340} is the fluorescence excited at 340 nm from the specimen cell (identical value in eq 1). Subtraction of

bleed-through from the total emission through each FRET-related cube permitted corrected FRET intensities to be obtained:

$$F_{CFP(C,Y)} \text{ or } F_{YFP(C,Y)} \text{ or } F_{FRET(C,Y)} = F_{CFP(F2,C,Y)} \text{ or } F_{YFP(F2,C,Y)} \text{ or } F_{FRET(F2,C,Y)} - F_{CFP(F2)calc} \text{ or } F_{YFP(F2)calc} \text{ or } F_{FRET(F2)calc} \quad (3)$$

After this correction of Fura-2 bleed-through, the FRET ratio (FR) was finally calculated according to the "three-cube" method described by Erickson et al.:[10]

$$FR = [F_{FRET(C,Y)} - R_{D1}F_{CFP(C,Y)}]/R_A[F_{YFP(C,Y)} - R_{D2}F_{FRET(C,Y)}] \quad (4)$$

The definitions of constants R_{D1}, R_{D2}, and R_A are as follows: $R_{D1} = F_{FRET(C)}/F_{CFP(C)}$, $R_{D2} = F_{YFP(C)}/F_{CFP(C)}$, and $R_A = F_{FRET(Y)}/F_{YFP(Y)}$. They were predetermined from measurements in single cells expressing only seCFP- or seYFP-tagged molecules. Because the correction was not made before the FRET calculation, it is worth emphasizing that this correction approach can be applied not only for this three-cube FRET calculation but also for other sensitized FRET calculations.[19−25]

Assessment of Calcium and FRET Relationships. $[Ca^{2+}]_i$−FR relationships under steady-state conditions in living cells were assessed at room temperature (20−25 °C). To quantitatively describe the relationship between $[Ca^{2+}]_i$ (determined by the Fura-2 ratio) and corrected FR, we adopted the following Hill fitting:

$$FR = \Delta FR_{max}[Ca^{2+}]_i^{\,n}/(K_{1/2}{}^n + [Ca^{2+}]_i^{\,n}) + FR_{basal} \quad (5)$$

To simulate the bell-shaped $[Ca^{2+}]_i$−FR relationship for seYFP-TRPC6CBD versus seCFP-CaMwt, a double Hill-based function was applied as follows:

$$FR = \Delta FR_{max}[Ca^{2+}]_i^{\,n}/(K_{1/2}{}^n + [Ca^{2+}]_i^{\,n}) - \Delta FR_{dmax}[Ca^{2+}]_i^{\,n}/(K_{1/2}{}^n + [Ca^{2+}]_i^{\,n}) + FR_{basal} \quad (6)$$

The $[Ca^{2+}]_i$ value was estimated using Grynkiewicz's equation with intracellular Fura-2 calibration values:[26] $[Ca^{2+}]_i = K_d'S_f(r - r_{min})/(r_{max} - r)$, where K_d' is the apparent dissociation constant of Fura-2, r is an interest F_{340}/F_{360} value, r_{min} is the minimum value of r obtained with zero Ca^{2+} calibrating solution, and r_{max} is the maximum value of r obtained with 39 μM free Ca^{2+}. K_d' was set to 225 nM. S_f is a slope factor. To obtain these constants, we used a magnesium-containing calcium calibration kit supplied by Molecular Probes.

Binding Analysis for CaM versus the Ion Channel Domain. Binding analysis was conducted on the basis of a 1:1 ligand binding model that is thought to determine two parameters: $\Delta FR_{max}'$ and $K_{d,EFF}$. $\Delta FR_{max}'$ is the maximum FR that occurs when all acceptor-tagged molecules are bound; hence, $\Delta FR_{max}'$ depends on only interfluorophore geometry. The second parameter, $K_{d,EFF}$, the effective dissociation constant, furnishes the relative dissociation constant for the binding reaction. The approximate conversion factor is 1×10^{-11} M for the actual K_d determined by dansylated CaM versus target binding analysis from previous studies.[4,27] The analysis basically followed the description in ref 4. However, we have omitted the value of 2 in eq A24, because of cytosolic protein−protein interactions not located in membrane cytosolic fractions. "gfA" and "gfD" fitting parameters are 0.010 and 0.121, respectively. The molar extinction ratio of seYFP and seCFP is 0.113. The quantum yield and molar extinction coefficient of seCFP, which we must know for the binding analysis, were determined as described in the Supporting Information.

RESULTS

Cross-Talk between Fura-2 and Fluorescent Proteins. Because there is certain cross-talk in excitation spectra of Fura-2 and seCFP (that of seYFP is relatively well-separated), we first considered the extent of cross-excitation of seCFP during Fura-2 ratiometric measurements (region 1 in Figure 1A). The seCFP fluorescence was captured from the Fura-2 cube through Fura-2 excitation filters at 340, 360, and 380 nm, in HEK293 cells expressing only seCFP. Plotting the seCFP fluorescence from the Fura-2 filter at three different excitation wavelengths [$F_{340(C)}$, $F_{360(C)}$, or $F_{380(C)}$] versus that from the CFP cube [$F_{CFP(C)}$] shows that a fluorescence equivalent to ∼15% of F_{CFP} artifactually bleeds through the Fura-2 cube with 380 nm excitation (blue). By contrast, this value is only marginal at 360 and 340 nm, being 2 and 0.3%, respectively (Figure 1B). The pair of F_{340} and F_{380} is most frequently used for ratiometric Ca^{2+} imaging because of its broad working range. However, the 15% increment in the F_{380} value would introduce an erroneous reduction in the apparent F_{340}/F_{380} ratio, which may then render subtle changes that cannot be easily detected, especially around the basal Ca^{2+} level. Furthermore, fluorescence signals from FRET and CFP cubes will contain considerable Ca^{2+}-dependent bleed-through of Fura-2 fluorescence that appears to be most serious at an excitation wavelength of 380 nm (Figure 1A). To minimize these two types of errors, we employed the pair of F_{340} and F_{360} throughout the following ratiometric $[Ca^{2+}]_i$ measurement. Nevertheless, the small differential bleed-through (slightly more on F_{360}) caused a slight reduction in the calculated value of $[Ca^{2+}]_i$. Typical reduction at the basal $[Ca^{2+}]_i$ level was a few nanomolar compared with cells lacking seCFP expression. However, it is possible to offset this small bleed-through differential by adjusting conditions to favor equal bleed-throughs of $F_{340(C)}$ and $F_{360(C)}$ filters, i.e., by wider and narrower band-pass or higher and lower transmission of excitation filters, respectively.

In the next step, we considered correcting Ca^{2+}-dependent Fura-2 bleed-through onto three images of FRET (F_{CFP}, F_{YFP}, and F_{FRET}, region 2 in Figure 1A). To quantify this Fura-2 cross-excitation at each time point, we sequentially measured its fluorescence intensity in five filter settings in Fura-2-loaded cells [F_{340}, F_{360}, $F_{CFP(F2)}$, $F_{YFP(F2)}$, and $F_{FRET(F2)}$] and varied $[Ca^{2+}]_i$ in a graded manner, by applying various concentrations of Ca^{2+} in the bath with or without ionomycin, a selective Ca^{2+} ionophore. The values of $F_{CFP(F2)}$, $F_{YFP(F2)}$, and $F_{FRET(F2)}$ were then normalized to (or divided by) the corresponding F_{340} values obtained from the same captured set of images. Plotting the $F_{CFP(F2)}/F_{340}$, $F_{YFP(F2)}/F_{340}$ or $F_{FRET(F2)}/F_{340}$ ratio (R) versus the F_{340}/F_{360} ratio (or calculated $[Ca^{2+}]_i$ value) shows that the extent of Fura-2 fluorescence bleed-through on FRET signals monotonically increases as $[Ca^{2+}]_i$ decreases (symbols in Figure 1C), which can be well fitted with single-exponential decaying functions of $[Ca^{2+}]_i$ (curves in Figure 1C). The best-fit parameters for these curves can be renewed in every experiment by repeating the same procedures on each coverslip for Fura-2-loaded cells without seCFP or seYFP expression. Using these functions as the calibrations for the bleed-through of Fura-2 onto

the three FRET cubes, we could reasonably correct the value of F_{CFP}, F_{YFP}, or F_{FRET} in respective experiments at each time point of measurement or its corresponding F_{340}/F_{360} value (i.e., $[Ca^{2+}]_i$) (see Experimental Procedures).

Correction of the FRET Increment by Fura-2 Loading. Figure 2A shows a representative control C/Y FRET experiment in which $[Ca^{2+}]_i$ was sequentially changed via application of various concentrations of external Ca^{2+} and ionomycin, which allows a modestchange in $[Ca^{2+}]_i$ by passive depletion or replenishment.[28,29] Without correction for Fura-2 fluorescence superposition, the observed FRET ratio (FR_{obs}), which was defined as the fractional increase in seYFP emission due to FRET, deviated above 1.0. The extent of this deviation became more prominent at lower F_{340}/F_{360} ratios (gray circles), i.e., lower $[Ca^{2+}]_i$ values (empty blue circles). However, when the superposed Fura-2 fluorescence was subtracted by the method described above, the corrected FR (FR_{cor}) value stayed near 1.0 (filled blue circles), ensuring that FRET did not change virtually even during stepwise changes in $[Ca^{2+}]_i$. The difference between FR_{obs} and FR_{cor} became smaller as the Fura-2 ratio increased to >1.6 (~1 μM free Ca^{2+}), probably because of the shift of the Fura-2 spectrum toward shorter wavelengths at higher Ca^{2+} concentrations.

As summarized in Figure 2C, at low $[Ca^{2+}]_i$ levels (Fura-2 ratio of ~0.8), a statistically significant increase in FR (nearly 150%) was detected upon Fura-2 loading (middle column; FR_{obs} = 1.6 ± 0.08; n = 34) with respect to conditions without Fura-2 (left column; FR = 1.1 ± 0.05; n = 29). However, after the correction, this apparent increase is canceled (right column in Figure 2C; FR_{cor} = 1.1 ± 0.04; n = 34). Similarly, a smaller but significant FR increase (~105%) appeared with Fura-2 loading in a dimeric seCFP−seYFP fusion protein that already exhibited a robust static FRET signal (middle vs left columns in Figure 2D). However, this is also adequately eliminated by the correction method described above (right column in Figure 2D). These results collectively suggest that the correction of Fura-2 fluorescence bleed-through greatly increases the reliability of FRET measurement, especially around lower Fura-2 ratios or $[Ca^{2+}]_i$ values.

We also examined the possibility that FRET occurring between Fura-2 and seYFP may affect the Fura-2 ratio, by using the donor dequenching method.[30] Fura-2 intensities (F_{340} and F_{360}) were not enhanced (actual change being an ~10% reduction) by bleaching seYFP (near 40% reduction with a 10 min illumination at 535 nm), suggesting no transfer of fluorescence energy from Fura-2 to seYFP (data not shown). This strongly indicates that the observed FRET signal should derive from the specific interaction between seCFP and seYFP proteins.

In Vivo Ca^{2+} Titration for smMLCKp and CaMwt Binding. After in vivo validation of our correction strategy, we investigated its applicability to Ca^{2+}-dependent molecular interactions in living cells. For this purpose, we coexpressed seYFP−smMLCKp

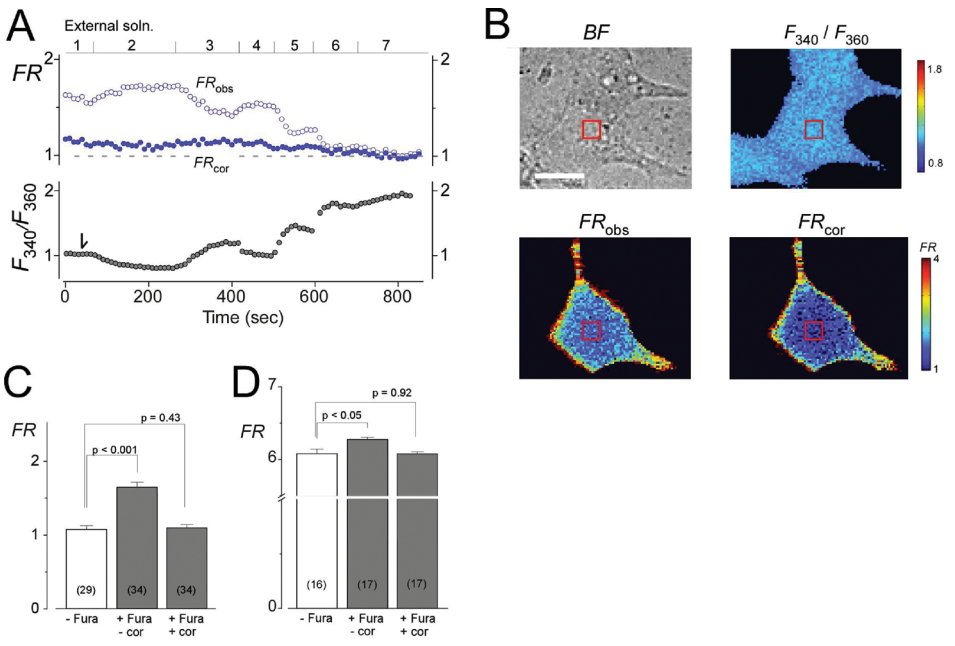

Figure 2. Evaluation for the correction approach to FRET measurement. (A) Time-lapse scatter plots of F_{340}/F_{360} (bottom) and FRET ratio (FR) (top). HEK cells coexpressing seCFP and seYFP proteins as separated molecules were loaded with Fura-2AM and then subjected to stepwise changes in external $CaCl_2$ concentration (0−10 mM) with or without ionomycin (1 or 5 μM). In the top and bottom panels, the Fura-2 ratio, the observed FR (FR_{obs}), and the corrected FR (FR_{cor}) are displayed as filled gray, empty blue, and filled blue circles, respectively. The numbers above the top panel indicate the external solutions [1, standard solution (1 mM Ca); 2, 1 mM EGTA (no Ca); 3, standard solution; 4, 1 μM Ca and 1 μM ionomycin (Io); 5, 1 μM Ca and 5 μM Io; 6, 3 μM Ca and 5 μM Io; 7, 10 μM Ca and 5 μM Io]. (B) Representative blight field (BF), Fura-2 ratio (F_{340}/F_{360}), FR_{obs}, and corrected FR (FR_{cor}, bottom right) images of HEK cells at the basal level of Ca^{2+}. The scale bar in BF represents 10 μm. Either Fura-2 or FR ratios are calculated from an averaged value at a fixed size ROI (region of interest, shown as a red square). (C) Fura-2 bleed-through correction for FR in cells cotransfected with seCFP and seYFP. Averaged FR from non-Fura-2-loaded cells (left), FR_{obs} from Fura-2-loaded cells (middle), and FR_{cor} from Fura-2-loaded cells with the correction (right). The numbers in parentheses indicate the number of cells tested. FR values (±standard error of the mean) from cells. (D) Correction on robust FR from the cells expressed with the seCFP−seYFP dimeric protein. The display setting is the same as that in panel C. Note when FR equals 1, no FRET is detected.

dx.doi.org/10.1021/bi200287x |*Biochemistry* 2011, 50, 4685–4696

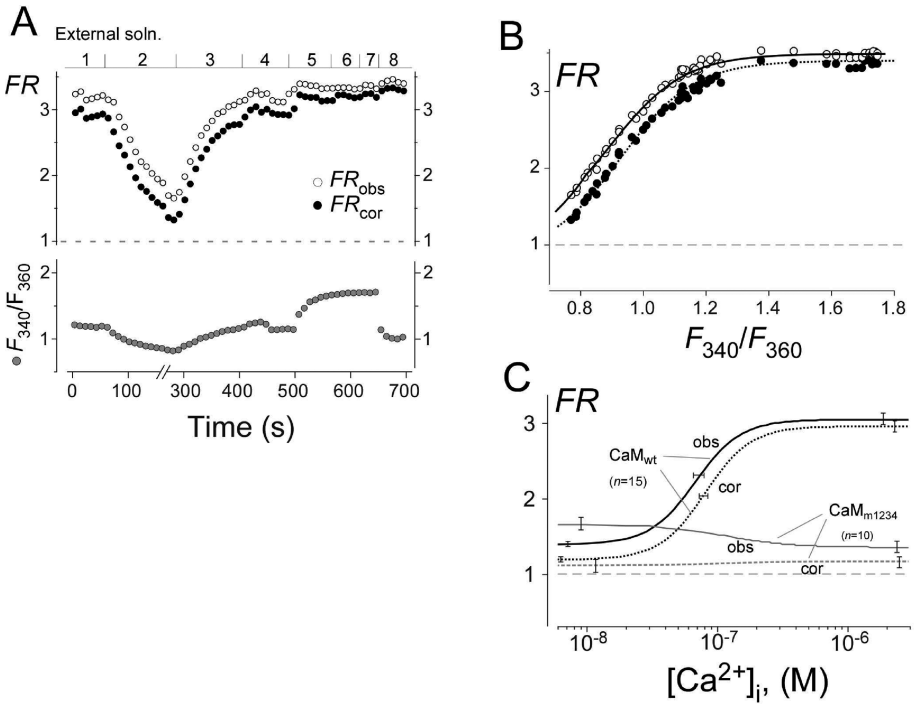

Figure 3. $[Ca^{2+}]_i$—FR relationship for seYFP—smMLCKp and seCFP—CaM fusion proteins from a living cell. (A) Fura-2 ratio (gray circles in the bottom panel) and FR_{obs} and FR_{cor} (empty and filled circles, respectively, in the top panel) were plotted vs time. $[Ca^{2+}]_i$ was sequentially changed via application of various external solutions that were same composition in Figure 2A (at number 8, Fura-2 was quenched by 10 mM Mn^{2+}). (B) Relationship between F_{340}/F_{360} and FR constructed from the time-lapse data shown in panel A. Smooth lines denote the absence of a hysteresis relationship in FR_{obs} (—) and FR_{cor} (···), suggesting a steady state. Fitting was done by eye. (C) Summary of $[Ca^{2+}]_i$—FR relationships showing Hill curves generated from the average of parameters from the Hill equation with nonlinear least-squares fits to individual data sets (CaMwt and CaM_{m1234}) (mean ± standard error of the mean).

Table 1. Steady-State Fitting Parameters[a] [observed (obs) vs corrected (cor)]

seYFP—smMLCK vs seCFP—X	ΔFR_{max}	Hill coefficient	$K_{1/2}$ ($\times 10^{-7}$ M)	FR_{basal}	n
CaM_{wt} (obs)	1.95 ± 0.15	2.39 ± 0.07	0.75 ± 0.07	1.30 ± 0.03	15
CaM_{wt} (cor)	1.76 ± 0.11	2.49 ± 0.06	0.80 ± 0.05	1.19 ± 0.02[b]	15
CaM_{m1234} (obs)	−0.16 ± 0.03	1.34 ± 0.16	2.06 ± 0.66	1.44 ± 0.14	10
CaM_{m1234} (cor)	0.09 ± 0.03[b]	1.52 ± 0.26	1.53 ± 0.56	1.18 ± 0.12[b]	10

[a] Results are expressed with the standard error of the mean. $K_{1/2}$ is the $[Ca^{2+}]_i$ at which FR is half-maximal, and FR_{basal} is the FR at which $[Ca^{2+}]_i$ is zero. Errors are compared with the observed and corrected values. Values are derived from the data shown in Figure 3C. [b] $p < 0.005$.

and seCFP—CaMwt fusion proteins in HEK cells, because their Ca^{2+}-dependent binding properties have been relatively well characterized. Figure 3A shows a typical experiment in which the rate of $[Ca^{2+}]_i$ elevation was greatly slowed ($\Delta F_{340}/F_{360} < 0.1$, or $\Delta[Ca^{2+}]_i$ = 10—100 nM per 10 s). In this way, we could equilibrate the $[Ca^{2+}]_i$—FR relationship to show no hysteresis (Figure 3B). The $[Ca^{2+}]$—FR relationship can be described well by the Hill equation (eq 5), with the maximal incremental and basal FR values (ΔFR_{max} and FR_{basal}, respectively), relative steepness [Hill coefficient (n) in eqs 5 and 6], and half-maximal $[Ca^{2+}]_i$ ($K_{1/2}$) (eq 5). The solid lines in Figure 3B show the best-fit results with the Hill equation for smMLCKp and CaMwt data (replotted from Figure 3A) before (○) and after (●) correction. Such data were pooled and averaged and are shown in Figure 3C (solid and dotted lines), together with the results for the Ca^{2+}-insensitive mutant (CaM_{m1234}) (solid and dotted gray lines in Figure 3C).

Regardless of the correction of Fura-2 bleed-through, recapitulation from 15 independent cells clearly demonstrates that CaMwt binds to smMLCK Ca^{2+}-dependently, and this property is only weak or absent for CaM_{m1234} (Figure 3C). However, for both CaMwt and CaM_{m1234}, corrected $[Ca^{2+}]_i$—FR relationships (dotted lines) give significantly smaller FR values than uncorrected ones (solid lines). In particular, the increased FR_{basal} value that reflects binding of Ca^{2+}-free CaM (or apoCaM) to the target almost disappeared (see also Table 1), and the apparent enhancement of FR_{obs} at low $[Ca^{2+}]_i$ values for CaM_{m1234} was almost completely eliminated (solid vs dotted gray lines in Figure 3C) by the correction. In contrast, the $K_{1/2}$ and n values for CaMwt are only modestly affected by the correction [changed from $(0.75 \pm 0.07) \times 10^{-7}$ M and 2.39 ± 0.07 to $(0.80 \pm 0.05) \times 10^{-7}$ M and 2.49 ± 0.06, respectively (Table 1)]. These results strongly suggest that this method may be most useful for evaluating the CaM—target binding around basal or relatively low $[Ca^{2+}]_i$ levels.

In addition, a Hill coefficient of >2 confirms that the process of Ca^{2+}-dependent binding of CaMwt to smMLCKp is positively cooperative, which is absent for CaM_{m1234} (Table 1). On the other hand, relatively large scatters in the ΔFR_{max} value may just reflect the variable stoichiometry and expression level of seCFP and seYFP molecules rather than variable concentrations of loaded Fura-2.

$[Ca^{2+}]_i$—FR Relationships of smMLCKp versus Partially Desensitized CaM Mutants (CaM_{m12} and CaM_{m34}) or CaM Mutants in the Hydrophobic Pockets (CaM_{F19A} and CaM_{F92A}). The Ca^{2+} binding constant for the seYFP—smMLCKp and seCFP—CaMwt pair obtained by our method [$K_{1/2} = 0.8 \times 10^{-7}$ M (Table 1)] is close to that reported in previous in vitro studies (0.3×10^{-7} M[31]). This fact encouraged us to further examine whether our experimental approach has enough potential to detect more subtle changes in the steady-state $[Ca^{2+}]$—FR relationship produced by functionally milder mutations in CaM. For this purpose, we first employed two seCFP-fused CaM mutants (CaM_{m12} and CaM_{m34}) that are partially desensitized to Ca^{2+} via monolobal mutations in the EF-hand motif. These mutations are known to cause the selective impairment of binding of Ca^{2+} to either the N-terminal (CaM_{m12}) or C-terminal (CaM_{m34}) lobe of CaM, thereby exhibiting unique differences in its Ca^{2+} affinity and function in a lobe-specific manner.[1] As shown in Figure 4, coexpression of the CaM mutant in EF-hands with smMLCKp caused significant rightward shifts in $[Ca^{2+}]_i$—FR relationships, with increased $K_{1/2}$ values for CaM_{m12} and CaM_{m34} (1.44×10^{-7} and 5.62×10^{-7} M, respectively; fitting parameters are summarized in Table 2). These data indicate that the impact of N-terminal lobe mutation is less prominent than C-terminal lobe mutation, being in good agreement with previous studies.[32,33]

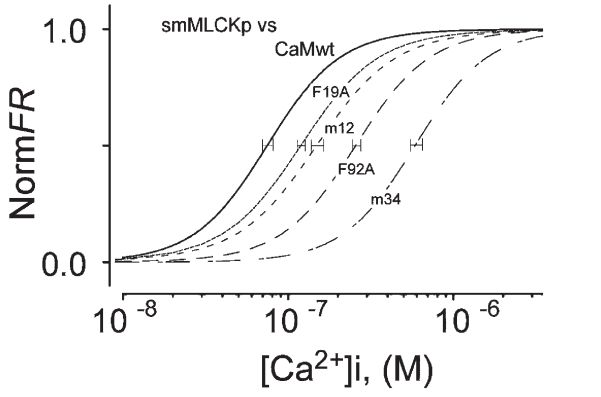

Figure 4. CaM mutants reveal the selective contribution for smMLCKp binding. Normalized $[Ca^{2+}]_i$—FR relationships for seYFP—smMLCKp fusion protein with seCFP—CaMwt (—), seCFP—CaM_{m12} (---), seCFP—CaM_{m34} (-—-), seCFP—CaM_{F19A} (· · ·), or seCFP—CaM_{F92A} (— — —) fusion protein. Fitting lines are generated from the average of parameters from the Hill equation to individual data (FR_{cor}) sets. Error bars indicate the standard error of the mean for the Ca^{2+} binding constant ($K_{1/2}$). Actual data parameters are listed in Table 2.

We then tested two single mutations of phenylalanine residues in respective lobe binding sites (i.e., hydrophobic pockets, CaM_{F19A} and CaM_{F92A}), which are also known to reduce the Ca^{2+} sensitivity of CaM. As anticipated, both mutants caused statistically significant rightward shifts in $[Ca^{2+}]_i$—FR relationships, but the extent is weaker than those of bi- or monolobal mutations [dotted and long-dash lines in Figure 4; $K_{1/2}$ values of $(1.12 \pm 0.06) \times 10^{-7}$ and $(2.42 \pm 0.07) \times 10^{-7}$ M for CaM_{F19A} and CaM_{F92A}, respectively (Table 2)].

The ability to distinguish small deviations in the $[Ca^{2+}]_i$—FR relationship described above [i.e., alteration of $K_{1/2}$ values as small as 30 nM (Table 2)] demonstrates a high fidelity of this method for detecting subtle changes in the interaction of CaM with target proteins in living cells. Furthermore, the other parameters obtained from the corrected relationships also point to an important possibility that the N-terminal lobe mutations in CaM would specifically impair its maximal binding strength at high $[Ca^{2+}]_i$ values (ΔFR_{max}) without affecting its positive cooperativity in Ca^{2+}-dependent binding (Hill coefficient of >2) and basal binding affinity ($FR_{basal} = 1.1—1.2$) (Table 2).

$[Ca^{2+}]_i$—FR Relationships for Channel Domain—CaM Binding. The Ca^{2+}-free and Ca^{2+}-dependent binding of CaM to ion channels is thought to be critical for their functional regulation and/or modulation. To understand it more quantitatively, we investigated the steady-state $[Ca^{2+}]_i$—FR relationships of CaM—channel binding over a wide range of $[Ca^{2+}]_i$ values using the approach described above. Toward this end, we coexpressed seCFP—CaMwt fusion protein and seYFP-fused CaM-binding regions from three types of voltage-gated channels and one isoform of the receptor-activated TRP channel in HEK293 cells.

As illustrated in Figure 5, the IQ domains (IQ is a consensus motif for CaM[34]) from voltage-gated channels ($Ca_V1.2$, $Ca_V2.1$, and $Na_V1.2$) all showed substantial FRET (FR_{basal}) at a very low $[Ca^{2+}]_i$ of 10^{-8} M. This strongly supports the idea that the IQ domain could serve as a tethering site for Ca^{2+}-free CaM or apoCaM,[10,27,35] and thus, significant association of CaM with the IQ domain is present even at the basal level of $[Ca^{2+}]_i$ ($\sim 1 \times 10^{-7}$ M). Consistent with this idea, tethering of apoCaM to voltage-dependent Ca channels has been proposed in electrophysiological studies with mutated CaM (CaM_{m1234}).[10] The binding of CaM to the IQ domains of two voltage-gated Ca channels ($Ca_V1.2$, the pore-forming subunit of the L-type Ca channel, or $Ca_V2.1$, the P/Q-type channel) is greatly enhanced

Table 2. Fitting Parameters[a] (corrected) for CaM Mutants vs smMLCKp

seYFP—smMLCKp vs seCFP—X	ΔFR_{max}	Hill coefficient	$K_{1/2}$ ($\times 10^{-7}$ M)	FR_{basal}	n
CaM_{m12}	1.47 ± 0.11^b	2.12 ± 0.07	1.47 ± 0.21^c	1.23 ± 0.03	7
CaM_{m34}	1.96 ± 0.18	3.12 ± 0.19^c	5.03 ± 0.26^c	1.27 ± 0.06	7
CaM_{F19A}	1.09 ± 0.27^c	2.36 ± 0.14	1.12 ± 0.06^c	1.17 ± 0.06	6
CaM_{F92A}	1.95 ± 0.17	2.88 ± 0.25^b	2.42 ± 0.07^c	1.18 ± 0.03	7

[a] Results are expressed with the standard error of the mean. Values are derived prior to normalization of data that is shown in Figure 4. Statistical analysis has been done compared with corrected values for smMLCKp vs wild-type CaM in Table 1. [b] $p < 0.05$. [c] $p < 0.005$.

with an increase in $[Ca^{2+}]_i$. However, the binding to the $Ca_V1.2$ IQ domain appears at a significantly lower $[Ca^{2+}]_i$ ($K_{1/2}$ = 1.13 ± 0.07 M^{-7}) than that of the $Ca_V1.2$ IQ domain ($K_{1/2}$ = 3.32 ± 0.22 M^{-7}) (see also Table 3).

CaM has also been identified as an associated protein controlling the gating and trafficking of the voltage-gated sodium channel ($Na_V1.X$).[36,37] The relative insensitivity of FRET to a wide range of $[Ca^{2+}]_i$ values (orange curve in Figure 5A) agrees well with our previous finding of equal or even stronger interaction of apoCaM with the $Na_V1.2$ IQ domain than Ca^{2+}-CaM at the steady state.[27] However, this C/Y-based FRET assay may not be sufficiently sensitive to detect dynamic structural changes between apoCaM−NaIQ and Ca^{2+}-CaM−NaIQ complexes, because the secondary structure profile previously investigated by circular dichroism indicates that drastic movement would occur from C-terminal lobe-specific association of apoCaM to bilobe association of Ca^{2+}-occupied CaM.[31]

The CaM binding domain (CBD) of TRPC6 (TRPC6CBD) shows a unique bell-shaped dependence for CaM binding on $[Ca^{2+}]_i$ with a peak around 600 nM (dashed line in Figure 5A). This biphasic $[Ca^{2+}]_i$ dependence is similar to that shown in a previous patch clamp study in which strong chelation of Ca^{2+} abolished the activation of TRPC6 channels by receptor stimulation.[38] The best fit of the $[Ca^{2+}]_i$−FR relationship with the double Hill equation indicates the positive cooperativity (Hill coefficient of ∼2) of Ca^{2+}-dependent binding of CaM to TRPC6CBD. This might reflect the lobe-specific binding of CaM to TRPC6CBD as observed for voltage-gated Ca channels. However, the FR increment at very low $[Ca^{2+}]_i$ values is only modest for TRPC6CBD (FR_{basal} ∼ 1.5), indicating that its lower binding affinity for apoCaM versus that of the IQ domains of voltage-gated channels, which is confirmed by binding analysis (see Figure 5 and Table 4).

Binding Analysis for Ca^{2+}-Dependent CaM−Channel Interaction. Finally, to understand the molecular basis of the observed FR changes, we employed the binding analysis[10] from the data in Figure 5 at low (30 nM), intermediate (500 nM), and high (2 μM) $[Ca^{2+}]_i$ levels in HEK cells expressing donor and acceptor molecules to varying extents (Figure 6). To simplify the interpretation of the observed data, we assumed a single-binding site model in which each channel fragment binds a single CaM molecule. Fitting of the relationships between FR and the relative concentration of free donor (seCFP−CaMwt) to this model suggests that the apparent binding constant ($K_{d,Eff}$), which is linearly correlated with the K_d of the donor−acceptor interaction,[4] changes with $[Ca^{2+}]_i$ differentially among different types of channel CaM binding domains (Figure 6).

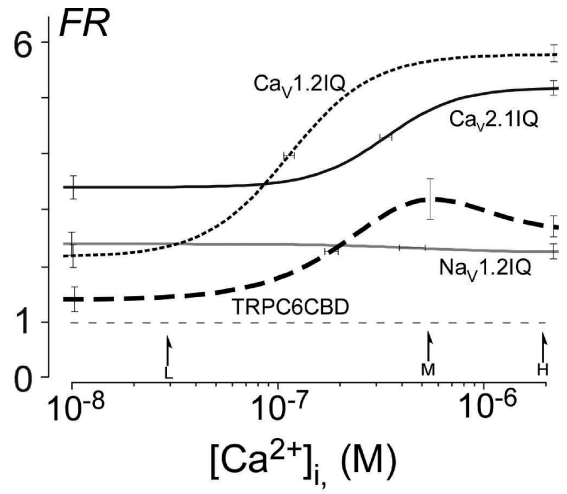

Figure 5. $[Ca^{2+}]_i$−FR relationships for CaMwt with ion channel domains for the interaction of seCFP−CaMwt fusion protein with seYFP−$Ca_V2.1$IQ (—; n = 16), seYFP−$Ca_V1.2$IQ (···; n = 8), seYFP−$Na_V1.2$IQ (gray line; n = 6), and seYFP−TRPC6CBD (−−−; n = 10) peptides. The half-arrowheads denote the approximate data points for the binding analysis at low, intermediate, and high Ca^{2+} concentrations. To produce those averaged lines, we used corrected FR values (FR_{cor}).

Table 4. Binding Parameters[a]

seCFP−CaMwt vs seYFP−X	$[Ca^{2+}]_i$	$K_{d,Eff}$	$\Delta FR_{max}'$	n
smMLCKp	L	557500 ± 134700	7.8 ± 2.1	15
	H	2900 ± 1300	6.0 ± 0.4	
$Ca_V1.2$ IQ	L	6800 ± 3100	5.2 ± 0.3	8
	H	4900 ± 1900	6.5 ± 0.4	
$Ca_V2.1$ IQ	L	23100 ± 2000	7.7 ± 0.3	16
	H	13200 ± 2300	7.9 ± 0.4	
$Na_V1.2$ IQ	L	10600 ± 3100	7.5 ± 0.4	6
	H	12500 ± 3600	7.2 ± 0.3	
TRPC6CBD	L	149000 ± 107500	4.4 ± 1.3	10
	M	16700 ± 3700	6.0 ± 0.5	
	H	33000 ± 10300	7.8 ± 0.9	

[a] Parameters associated with fits of the binding model to FRET data for indicated donor and acceptor pairs at low (L, 0.03 μM), intermediate (M, 0.5 μM), and high (H, 2 μM) free approximate Ca^{2+} concentrations. $K_{d,EFF}$ is the relative dissociation constant. $\Delta FR_{max}'$ is the fractional increase in seYFP emission due to FRET when all seYFP-tagged molecules are bound with seCFP-tagged molecules. Data for seYFP−smMLCKp fusion protein was taken from Figure 3. Means ± the standard error give 68% confidence intervals, as determined by the inverse of the F probability distribution.[48]

Table 3. Fitting Parameters[a] (corrected) for CaM_{wt} vs Ion Channel Targets

seYFP−X vs seCFP−CaMwt	ΔFR_{max}	Hill coefficient	$K_{1/2}$ (×10^{-7} M)	FR_{basal}	n
$Ca_V1.2$ IQ	3.64 ± 0.15	2.14 ± 0.14	1.13 ± 0.07	2.22 ± 0.24	8
$Ca_V2.1$ IQ	1.80 ± 0.07	2.48 ± 0.07	3.32 ± 0.22	3.47 ± 0.30	16
$Na_V1.2$ IQ	−0.15 ± 0.12	1.91 ± 0.34	2.45 ± 0.21	2.46 ± 0.21	6
TRPC6CBD	6.52 ± 0.48	1.74 ± 0.07	4.03 ± 0.30	1.49 ± 0.12	10
	5.26 ± 0.52	1.98 ± 0.04	6.27 ± 0.45		

[a] Values are derived from the data shown in Figure 5. The means of all parameters are significantly different on the basis of one-way ANOVA (p < 0.005).

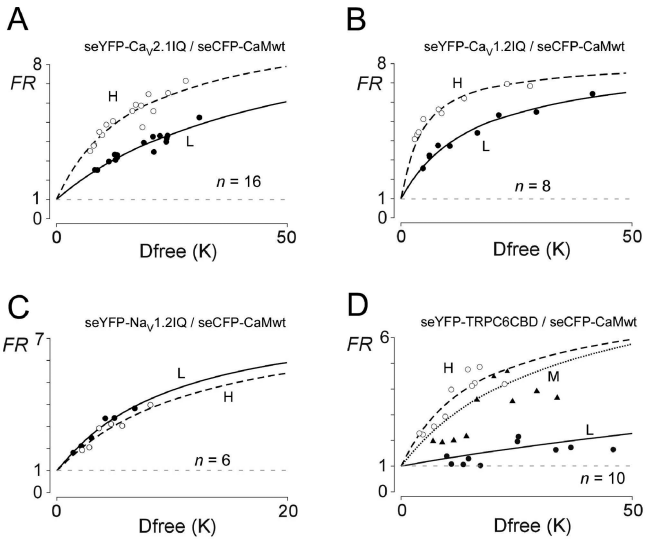

Figure 6. Binding analysis for CaM and ion channel domains at different $[Ca^{2+}]_i$ levels. The Ca^{2+}-dependent FRET strength (FR) determined for each cell [low (L) (●), middle (M) (▲), and high (H) (○) F_{340}/F_{360} values in Figure 5A] is plotted vs the free relative donor (seCFP−CaMwt) concentration, D_{free}. FRET strengths increase as the fraction of seYFP−channel targets bound to seCFP−CaM increase with an increasing concentration of free seCFP−CaM ($\sim D_{free}$, in relative units). Fitting parameters are listed in Table 3.

As summarized in Table 4, for the interaction of CaM with the IQ domains from $Ca_V2.1$ and $Ca_V1.2$, the values of $K_{d,Eff}$ are enhanced 2- and 3-fold, respectively, by an increase in $[Ca^{2+}]_i$ from 30 nM to 2 μM. In contrast, the $K_{d,Eff}$ for the $Na_v1.2$IQ domain indicates no or slightly inverse correlation with $[Ca^{2+}]_i$, and that for TRPC6CBD exhibits a biphasic $[Ca^{2+}]_i$ dependence with the highest affinity at an intermediate $[Ca^{2+}]_i$ level (500 nM). These results are consistent with those obtained by the steady-state $[Ca^{2+}]_i$−FR relationships. Thus, the observed FR change can be ascribed mostly to Ca^{2+}-dependent changes in the binding affinity of CaM rather than its spatial rearrangement. This affinity change is prominent for the CaM binding domains of L- and P/Q-type Ca and TRPC6 channels, but not for the sodium channel.

DISCUSSION

In this paper, we present two major developments utilizing Fura-2 and C/Y FRET imaging in single living cells: (1) a quantitative measurement of Fura-2 and C/Y FRET to minimize the cross-talk issue and (2) steady-state Ca^{2+}-dependent binding of CaM with smMLCKp and targets from various types of ion channels in intact cells. As the results of these experiments, substantial Ca^{2+}-dependent FRET changes can be obtained for the IQ domains of voltage-gated L- and P/Q-type Ca channels and the calmodulin binding domain (CBD) of the TRPC6 channel but not for the voltage-gated Na channel. The IQ domain of L-type Ca channels demonstrates a higher sensitivity to $[Ca^{2+}]_i$ than that of P/Q-type Ca channels. The CaM−target domains of three voltage-gated ion channels show robust CaM binding at basal or lowered Ca^{2+} levels (apoCaM), but this is weaker for TRPC6.

Quantitative Imaging of Fura-2 and C/Y FRET. Detection of multiple photochemical events from living cells has been a critical challenge in developing an in-depth understanding of biological functions. So far, this has been accomplished by the combined use of photoprobes that can measure respective cellular events with high specificity and fidelity. However, to use multiple photoprobes with the least photochemical interference, it is frequently necessary to introduce adequate correction methods, because the emission and excitation spectra of chemical compounds or protein probes often overlap. In this respect, our approach provides a simple, readily feasible, and generalizable method for offsetting the obfuscating cross-excited fluorescence, which will work especially powerfully in the detection of several hundred nanomolar or even a changes of a lower magnitude in $[Ca^{2+}]_i$. For the future, combination of C/Y FRET and Fura-2 derivatives (e.g., Fura-6F, suitable for higher Ca^{2+} concentrations) or chemical probes is poised to become a promising strategy, because a wealth of unique FRET probes and chemical probes have been created: cell signaling sensors, voltage-sensing dyes, reactive oxygen species probes, and indicators for ions other than Ca^{2+}, such as Mg^{2+} and Na^+. Thus, our method may help to improve the resolution of detecting a variety of biological signals by means of photochemical imaging techniques.

Steady-State $[Ca^{2+}]_i$−FR Relationship in Living Cells. To thoroughly understand the complicated process of Ca^{2+}-dependent CaM regulations on ion channels or other molecules and its functionality in living cells, numerous factors need to be considered such as concentrations and diffusions of Ca^{2+}, CaM, and target molecules, their binding kinetics, endogenous protein disturbances, and other cytosolic circumstances. One of the critical factors in this steady-state experiment would be the kinetic imbalance between K_{on} and K_{off} for CaM−target binding. Differences from ten- to several hundred-fold in apparent association and dissociation constants of apoCaM with the Ca^{2+}-occupied complex have been potentially presented.[39] In fact, we occasionally observed that a significant "hysteresis" has emerged when $[Ca^{2+}]_i$ uptake and depletion occurred too quickly, which is probably due to the differential kinetics.[40,41] Therefore, it may be necessary to more carefully control the rate of $[Ca^{2+}]_i$ change in intact cells than in permeabilized cells. Nevertheless, our successful construction of steady-state $[Ca^{2+}]_i$−FR relationships in living cells is a promising tool for revealing a more physiologically linked mechanistic understanding of CaM functions. It should also be emphasized that, if experimental protocols are adequately designed and carefully implemented, our method could practically be applied to most types of intact cells and extended to quantifying the steady-state relationships between $[Ca^{2+}]_i$ and various protein−protein interactions therein.

Physiological Impact of the CaM Regulations on Ion Channels. The variability of Ca^{2+}-dependent constants, $K_{1/2}$ (Figure 5 and Table 3), can differentially implicate Ca^{2+}-CaM-mediated regulation of ion channels in physiological functions and pathophysiological consequences. For example, the observed Ca^{2+}-dependent FRET enhancement of the P/Q-type Ca channel IQ domain at higher $[Ca^{2+}]_i$ levels compared to that of L-type Ca channels, despite the functional outcome still being unclear, may correspond to the inactivation and/or facilitation of the channel occurring at high $[Ca^{2+}]_i$ levels.[42] This could in turn allow the fast Ca^{2+}-dependent facilitation or inactivation of the P/Q-type Ca^{2+} channel, thereby fine-tuning the amount of neurotransmitter released from the synaptic bottom.

$Na_V1.2$, a pore-forming subunit of voltage-gated neuronal sodium channels, exhibits constitutive binding of apo-CaM or Ca^{2+}-CaM through the IQ domain in the C-terminus. In recent work, Chagot and Chazin[43] determined the structure of the cardiac sodium channel $Na_V1.5$ IQ−CaM complex under calcium-free conditions by NMR. The results showed that the $Na_V1.5$ IQ domain interacts with the C-terminal domain of CaM, with the N-terminal lobe left free in solution. In a previous report, we found that only the truncated C-terminal lobe could largely induce α-helical contents (almost 2 times) by applying $Na_V1.2$ IQ peptides but not the N-terminal lobe.[31] Recent work by Feldkamp et al. described more details about this observation in which the high degree of similarity between apoCaM−$Na_V1.2$ IQ structures and that of $Na_V1.5$ IQ has been demonstrated.[44] However, it still remains unclear how the complex of the Na_V IQ domain and Ca^{2+}-CaM is structurally arranged, where a contribution of both lobes is predicted to produce the channel modulation.[45−47]

The bell-shaped relationship of the TRPC6CBD−CaM complex is even more intriguing, because the activation curve of the TRPC6 channel is expressed with a closely similar bell shape for cytosolic Ca^{2+}.[38] Although the peak of this Ca^{2+} dependence is slightly lower (∼200 nM) than our values, the cooperativity factor estimated from published data (Hill coefficient of ∼2.4) is close to that obtained from the $[Ca]_i$−FR relationship. Such similarity suggests that Ca^{2+}-dependent formation of the CaM−TRPC6 complex may underlie its Ca^{2+}-dependent activation. In addition, while a substantial proportion of CaM is associated with at least three distinct types of voltage-gated ion channels at basal or sub-basal $[Ca^{2+}]_i$ levels, the association of TRPC6CBD and wild-type CaM demonstrated a significant but only small FR increment at a sub-basal $[Ca^{2+}]_i$ of 10^{-8} M [FR_{basal} = 1.49 ± 0.12; n = 10; p < 0.05 compared with the control FR (C/Y)]. This small increment of FR_{basal} was almost same as that of the Ca^{2+}-insensitive CaM mutant (CaM_{m1234}) [1.42 ± 0.08; n = 7; p < 0.05 (data not shown)]. These results suggest relatively weak binding of apoCaM to TRPC6CBD. Our previous research also had demonstrated the dominant negative effect of CaM_{m1234} on the activation of the TRPC6 channel. We thus expected to detect substantial FRET between TRPC6CBD and CaM even at the basal $[Ca^{2+}]_i$ level. One simplistic explanation for this apparent contradiction is that despite its weak binding affinity, a dominating amount of overexpressed CaM_{m1234} compared to endogenous CaM could cause an unphysiologically high occupancy of TRPC6CBD, which may then impair the activation of the TRPC6 channel. In aggregate, under a physiological condition that precipitates less CaM accumulation near the membrane, tethering of CaM may play a weaker role in TRPC6 channel regulation than in those voltage-gated ion channels.

Linear Relation between the Ca^{2+}-CaM−Target Binding Constant and the Ca^{2+} Constant. A recent mathematical approach by Valeyev et al. suggests that the target specificity and selectivity of CaM-mediated regulation can be ascribed to variations in the number of Ca^{2+} ions required for target activation, the order of Ca^{2+}-CaM−target complex assembly, and dissociation constants cooperatively affected by respective Ca^{2+} binding steps.[3] To gain more insight into our results in light of this model, we plotted the maximally effective binding constants for CaM and CaM binding domains ($K_{d,EFF}$), which can be obtained at a very high $[Ca^{2+}]_i$ level [or a medium level for TRPC6CBD (Figure 5)], against the Ca^{2+} dissociation constant for cooperative CaM−target binding ($K_{1/2}$) derived from $[Ca^{2+}]_i$−FR relationships, for MLCK, three voltage-gated channels, and the TRPC6 channel (Figure 7). Somewhat surprisingly, a nearly linear correlation was found between these two constants. This implies that the binding of Ca^{2+}-CaM to the CaM binding domain may primarily contribute to the overall degree of formation of the Ca^{2+}-dependent CaM−target complex. However, our plotted data cover only a small range, not known in extra robust or weak association target areas. That may be critical for the cooperative binding processes of Ca^{2+}, CaM, and target proteins.

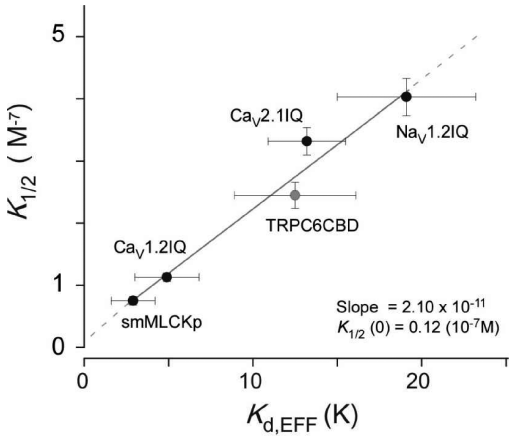

Figure 7. Linear relationship between dissociation constants and macroscopic Ca^{2+} effect ($K_{1/2}$). Symbols (●) correspond to means ± the standard error of the mean for data from CaM and smMLCKp or ion channel CaM binding targets at high Ca^{2+} concentrations (gray circle for TRPC6CBD with an intermediate Ca^{2+} concentration).

The results described so far are derived solely from the isolated regions of ion channels rather than intact whole channel proteins. It is thus still uncertain whether the observed characteristics of $[Ca^{2+}]_i$−FR relationships hold for intact ion channels. Nevertheless, several examples shown above would emphasize that our system has a promising potential to measure Ca^{2+}-dependent constants for the formation of the CaM−channel protein complex. Further refinement of Fura-2 and C/Y FRET imaging techniques, such as a high-speed filter exchanger or even highly sensitized fluorescence microscopy, will facilitate physiological significance of a broader range of cellular signals when these are intimately associated with changes in cytosolic $[Ca^{2+}]_i$.

■ ASSOCIATED CONTENT

Supporting Information. Construction and amino acid sequences for CaM target molecules, typical fitting parameters of eq 1, purification of seCFP, and spectral characterization of seCFP. This material is available free of charge via the Internet at http://pubs.acs.org.

■ AUTHOR INFORMATION

Corresponding Author

*Department of Physiology, School of Medicine, Fukuoka University, 7-45-1 Nanakuma, Johnan-ku, Fukuoka City, Fukuoka 814-0180, Japan. Phone: +81(92)801-1011. Fax: +81(92)614-8269. E-mail: mxmori@fukuoka-u.ac.jp.

Funding Sources

This work was supported by a Grant-in-Aid for Young Scientists (M.X.M.) from the Japan Society for the Promotion of Sciences and the Naito Foundation (M.X.M.).

■ ACKNOWLEDGMENT

We are grateful to Dr. Henry W. Colecraft for comments on our manuscripts, Dr. Todoroki Kenichiro for technical assistance with fluorescence photometers, and Dr. Jun Ichikawa for help with microscopic maintenance and discussions. We thank many researchers who supplied plasmids (see Experimental Procedures).

■ ABBREVIATIONS

CaM, calmodulin; CBD, calmodulin binding domain; FRET, fluorescence or Förster resonance energy transfer; Fura-2 AM, Fura-2 acetoxymethyl ester; seCFP, superenhanced cyan fluorescent protein; seYFP, superenhanced yellow fluorescent protein; smMLCKp, smooth muscle myosin light chain kinase CaM binding peptide; TRPC6, transient receptor for potential canonical 6.

■ REFERENCES

(1) Saimi, Y., and Kung, C. (2002) Calmodulin as an ion channel subunit. *Annu. Rev. Physiol. 64*, 289–311.

(2) Haeseleer, F., Imanishi, Y., Sokal, I., Filipek, S., and Palczewski, K. (2002) Calcium-binding proteins: Intracellular sensors from the calmodulin superfamily. *Biochem. Biophys. Res. Commun. 290*, 615–623.

(3) Valeyev, N. V., Bates, D. G., Heslop-Harrison, P., Postlethwaite, I., and Kotov, N. V. (2008) Elucidating the mechanisms of cooperative calcium-calmodulin interactions: A structural systems biology approach. *BMC Syst. Biol. 2*, 48.

(4) Erickson, M. G., Liang, H., Mori, M. X., and Yue, D. T. (2003) FRET two-hybrid mapping reveals function and location of L-type Ca^{2+} channel CaM preassociation. *Neuron 39*, 97–107.

(5) Imredy, J. P., and Yue, D. T. (1992) Submicroscopic Ca^{2+} diffusion mediates inhibitory coupling between individual Ca^{2+} channels *Neuron 9*, 197–207.

(6) Bers, D. M. (2008) Calcium cycling and signaling in cardiac myocytes. *Annu. Rev. Physiol. 70*, 23–49.

(7) Bezprozvanny, I., and Mattson, M. P. (2008) Neuronal calcium mishandling and the pathogenesis of Alzheimer's disease. *Trends Neurosci. 31*, 454–463.

(8) Parekh, A. B. (2010) Store-operated CRAC channels: Function in health and disease. *Nat. Rev. Drug Discovery 9*, 399–410.

(9) Vogel, S. S., Thaler, C., and Koushik, S. V. (2006) Fanciful FRET. *Sci. STKE 331*, re2.

(10) Erickson, M. G., Alseikhan, B. A., Peterson, B. Z., and Yue, D. T. (2001) Preassociation of calmodulin with voltage-gated Ca^{2+} channels revealed by FRET in single living cells. *Neuron 31*, 973–985.

(11) Zal, T., and Gascoigne, N. R. (2004) Photobleaching-corrected FRET efficiency imaging of live cells. *Biophys. J. 86*, 3923–3939.

(12) Tay, L. H., Griesbeck, O., and Yue, D. T. (2007) Live-cell transforms between Ca^{2+} transients and FRET responses for a troponin-C-based Ca^{2+} sensor. *Biophys. J. 93*, 4031–4040.

(13) Wier, W. G., Rizzo, M. A., Raina, H., and Zacharia, J. (2008) A technique for simultaneous measurement of Ca^{2+}, FRET fluorescence and force in intact mouse small arteries. *J. Physiol. 586*, 2437–2443.

(14) Harbeck, M. C., Chepurny, O., Nikolaev, V. O., Lohse, M. J., Holz, G. G., and Roe, M. W. (2006) Simultaneous optical measurements of cytosolic Ca^{2+} and cAMP in single cells. *Sci. STKE 353*, pl6.

(15) Carlson, H. J., and Campbell, R. E. (2009) Genetically encoded FRET-based biosensors for multiparameter fluorescence imaging. *Curr. Opin. Biotechnol. 20*, 19–27.

(16) Zacharias, D. A., Violin, J. D., Newton, A. C., and Tsien, R. Y. (2002) Partitioning of lipid-modified monomeric GFPs into membrane microdomains of live cells. *Science 296*, 913–916.

(17) Itoh, R. E., Kurokawa, K., Ohba, Y., Yoshizaki, H., Mochizuki, N., and Matsuda, M. (2002) Activation of rac and cdc42 video imaged by fluorescent resonance energy transfer-based single-molecule probes in the membrane of living cells. *Mol. Cell. Biol. 22*, 6582–6591.

(18) Nagai, T., Ibata, K., Park, E. S., Kubota, M., Mikoshiba, K., and Miyawaki, A. (2002) A variant of yellow fluorescent protein with fast and efficient maturation for cell-biological applications. *Nat. Biotechnol. 20*, 87–90.

(19) Chen, H., Puhl, H. L., Koushik, S. V., Vogel, S. S., and Ikeda, S. R. (2006) Measurement of FRET efficiency and ratio of donor to acceptor concentration in living cells. *Biophys. J. 91*, 39–41.

(20) Gordon, G. W., Berry, G., Liang, X. H., Levine, B., and Herman, B. (1998) Quantitative fluorescence resonance energy transfer measurements using fluorescence microscopy. *Biophys. J. 74*, 2702–2713.

(21) Miyawaki, A., Llopis, J., Heim, R., McCaffery, J. M., Adams, J. A., Ikura, M., and Tsien, R. Y. (1997) Fluorescent indicators for Ca^{2+} based on green fluorescent proteins and calmodulin. *Nature 388*, 882–887.

(22) Sorkin, A., McClure, M., Huang, F., and Carter, R. (2000) Interaction of EGF receptor and grb2 in living cells visualized by fluorescence resonance energy transfer (FRET) microscopy. *Curr. Biol. 10*, 1395–1398.

(23) Vanderklish, P. W., Krushel, L. A., Holst, B. H., Gally, J. A., Crossin, K. L., and Edelman, G. M. (2000) Marking synaptic activity in dendritic spines with a calpain substrate exhibiting fluorescence resonance energy transfer. *Proc. Natl. Acad. Sci. U.S.A. 97*, 2253–2258.

(24) Xia, Z., and Liu, Y. (2001) Reliable and global measurement of fluorescence resonance energy transfer using fluorescence microscopes. *Biophys. J. 81*, 2395–2402.

(25) Zal, T., Zal, M. A., and Gascoigne, N. R. (2002) Inhibition of T cell receptor-coreceptor interactions by antagonist ligands visualized by live FRET imaging of the T-hybridoma immunological synapse. *Immunity 16*, 521–534.

(26) Grynkiewicz, G., Poenie, M., and Tsien, R. Y. (1985) A new generation of Ca^{2+} indicators with greatly improved fluorescence properties. *J. Biol. Chem. 260*, 3440–3450.

(27) Mori, M., Konno, T., Ozawa, T., Murata, M., Imoto, K., and Nagayama, K. (2000) Novel interaction of the voltage-dependent sodium channel (VDSC) with calmodulin: Does VDSC acquire calmodulin-mediated Ca^{2+}-sensitivity?. *Biochemistry 39*, 1316–1323.

(28) Manor, D., Moran, N., and Segal, M. (1994) Interactions among calcium compartments in C6 rat glioma cells: Involvement of potassium channels. *J. Physiol. 478* (Part 2), 251–263.

(29) Smyth, J. T., Dehaven, W. I., Jones, B. F., Mercer, J. C., Trebak, M., Vazquez, G., and Putney, J. W., Jr. (2006) Emerging perspectives in store-operated Ca^{2+} entry: Roles of Orai, Stim and TRP. *Biochim. Biophys. Acta 1763*, 1147–1160.

(30) Bastiaens, P. I., Majoul, I. V., Verveer, P. J., Soling, H. D., and Jovin, T. M. (1996) Imaging the intracellular trafficking and state of the AB5 quaternary structure of cholera toxin. *EMBO J. 15*, 4246–4253.

(31) Mori, M., Konno, T., Morii, T., Nagayama, K., and Imoto, K. (2003) Regulatory interaction of sodium channel IQ-motif with calmodulin C-terminal lobe. *Biochem. Biophys. Res. Commun. 307*, 290–296.

(32) Johnson, J. D., Snyder, C., Walsh, M., and Flynn, M. (1996) Effects of myosin light chain kinase and peptides on Ca^{2+} exchange with the N- and C-terminal Ca^{2+} binding sites of calmodulin. *J. Biol. Chem. 271*, 761–767.

(33) Shuman, C. F., Jiji, R., Kerfeldt, K. S., and Linse, S. (2006) Reconstitution of calmodulin from domains and subdomains: Influence of target peptide. *J. Mol. Biol. 358*, 870–881.

(34) Rhoads, A. R., and Friedberg, F. (1997) Sequence motifs for calmodulin recognition. *FASEB J. 11*, 331–340.

(35) Lee, A., Zhou, H., Scheuer, T., and Catterall, W. A. (2003) Molecular determinants of Ca^{2+}/calmodulin-dependent regulation of $Ca_v2.1$ channels. *Proc. Natl. Acad. Sci. U.S.A. 100*, 16059–16064.

(36) Biswas, S., Deschenes, I., Disilvestre, D., Tian, Y., Halperin, V. L., and Tomaselli, G. F. (2008) Calmodulin regulation of Nav1.4 current: role of binding to the carboxyl terminus. *J. Gen. Physiol. 131*, 197–209.

(37) Potet, F., Chagot, B., Anghelescu, M., Viswanathan, P. C., Stepanovic, S. Z., Kupershmidt, S., Chazin, W. J., and Balser, J. R. (2009) Functional Interactions between Distinct Sodium Channel Cytoplasmic Domains through the Action of Calmodulin. *J. Biol. Chem. 284*, 8846–8854.

(38) Shi, J., Mori, E., Mori, Y., Mori, M., Li, J., Ito, Y., and Inoue, R. (2004) Multiple regulation by calcium of murine homologues of transient receptor potential proteins TRPC6 and TRPC7 expressed in HEK293 cells. *J. Physiol. 561*, 415–432.

(39) Peersen, O. B., Madsen, T. S., and Falke, J. J. (1997) Intermolecular tuning of calmodulin by target peptides and proteins: Differential effects on Ca^{2+} binding and implications for kinase activation. *Protein Sci. 6*, 794–807.

(40) Black, D. J., Selfridge, J. E., and Persechini, A. (2007) The kinetics of Ca^{2+}-dependent switching in a calmodulin-IQ domain complex. *Biochemistry 46*, 13415–13424.

(41) Tzortzopoulos, A., and Torok, K. (2004) Mechanism of the T286A-mutant αCaMKII interactions with Ca^{2+}/calmodulin and ATP. *Biochemistry 43*, 6404–6414.

(42) Nakamura, T., Yamashita, T., Saitoh, N., and Takahashi, T. (2008) Developmental changes in calcium/calmodulin-dependent inactivation of calcium currents at the rat calyx of Held. *J. Physiol. 586*, 2253–2261.

(43) Chagot, B., and Chazin, W. J. (2011) Solution NMR Structure of Apo-Calmodulin in Complex with the IQ Motif of Human Cardiac Sodium Channel NaV1.5. *J. Mol. Biol. 406*, 106–119.

(44) Feldkamp, M. D., Yu, L., and Shea, M. A. (2011) Structural and Energetic Determinants of Apo Calmodulin Binding to the IQ Motif of the NaV1.2 Voltage-Dependent Sodium Channel. *Structure*.

(45) Kim, J., Ghosh, S., Liu, H., Tateyama, M., Kass, R. S., and Pitt, G. S. (2004) Calmodulin mediates Ca^{2+} sensitivity of sodium channels. *J. Biol. Chem. 279*, 45004–45012.

(46) Theoharis, N. T., Sorensen, B. R., Theisen-Toupal, J., and Shea, M. A. (2008) The neuronal voltage-dependent sodium channel type II IQ motif lowers the calcium affinity of the C-domain of calmodulin. *Biochemistry 47*, 112–123.

(47) Biswas, S., DiSilvestre, D., Tian, Y., Halperin, V. L., and Tomaselli, G. F. (2009) Calcium-mediated dual-mode regulation of cardiac sodium channel gating. *Circ. Res. 104*, 870–880.

(48) Kemmer, G., and Keller, S. (2010) Nonlinear least-squares data fitting in Excel spreadsheets. *Nat. Protoc. 5*, 267–281.